A Thermal and Microstructure Evolution Model of Direct-Drive Friction Welding of Plain Carbon Steel

T.C. NGUYEN and D.C. WECKMAN

A model of direct-drive friction welding has been developed, which can be used to predict the time-temperature histories, the resultant microstructure, and the microhardness distribution across the weld interface of direct-drive friction-welded AISI/SAE 1045 steel bars. Experimentally measured power and axial displacement data were used in conjunction with a finite-element transient thermal model to predict the time-temperature history within the heat-affected zone (HAZ) of the weld. This was then used with a microstructure evolution model to predict the volume fraction of the subsequent microconstituents and the microhardness distribution across the weld interface of welds produced using three significantly different welding conditions: one with optimal conditions, one with a long burn-off time, and one with high axial pressure and rotational speed but short burn-off time. There was generally good agreement between the predicted and the measured time-temperature histories, volume fraction of the resultant microstructures, and microhardness distribution in the HAZ of AISI/SAE 1045 steel friction welds produced using these three significantly different welding conditions.

I. INTRODUCTION

DIRECT-DRIVE friction welding is a well-established solid-state joining process, which can be used to join a wide range of conventional steel alloys, as well as more metallurgically challenging systems such as dissimilar metal combinations and superalloys. Figure 1 illustrates the four basic stages in direct-drive friction welding. In the start-up stage, one work piece is clamped in a spindle and a variable speed DC motor is used to rotate it at a predetermined speed relative to a stationary work piece. To begin the heat-up stage, the two parts are brought together and an axial compressive force, F_1, is applied. Initially, heat is generated by friction at the faying surfaces. This raises the temperature of the metal at the weld interface and causes a decrease in the flow stress of the metal. When the flow stress of the heated metal at the weld interface becomes less than the applied axial compressive stress, the metal begins to plastically deform at a high strain rate. This plastic deformation now generates the heat at the interface. At the same time, the plastically deforming metal at the interface flows radially outward to create the flash, carrying with it any oxides and contaminants at the faying surfaces. This plastic flow of metal and formation of the flash occurs during the burn-off stage and results in axial displacement of both work pieces toward each other and shortening of the overall weldment. Finally, the welding process is completed during the forging stage by stopping all rotation and applying a high compressive force, F_3.

Friction welding has several advantages over conventional fusion welding processes. Since friction welding is a solid-state joining process, all defects associated with melting and solidification in a typical fusion weld are absent in a friction weld. During friction welding, the heat is highly concentrated at the weld interface. As a result, a friction weld has a very narrow heat-affected zone (HAZ), which limits the variations in mechanical properties of the base metal to a small region. Friction welding has the additional advantages that filler metal, flux, and shielding gas are not required and the cycle time of the process is very short; small parts take only a few seconds to weld. Finally, once a suitable welding procedure has been established, the resultant weld dimensions and high weld quality are very consistent and reproducible.

During friction welding of plain carbon and low-alloy steels, the metal within the HAZ of the weld is heated above the eutectoid temperature and transforms into austenite. At the end of the forging stage, this metal cools below the eutectoid temperature and the austenite decomposes into its various daughter products: ferrite, pearlite, bainite, or martensite.[1] The type and volume fraction of these final microconstituents are functions of the peak temperature reached during welding and the subsequent cooling rate. These will in turn determine the final strength and susceptibility of the weld to brittle fracture, as well as the need for postweld heat treatment.

The peak temperature and the cooling rate in the HAZ of a friction weld are extremely difficult to measure experimentally due to the severe plastic deformation that takes place at the weld interface. Alternatively, numerical modeling is a tool that can be used to gain insight and better understanding of the relationships between the welding process parameters, the thermal history in the HAZ, and the resultant weld microstructure. Furthermore, a model of friction welding can greatly reduce the time and the cost of developing a welding procedure for each new set of weld geometry and steel composition.

As shown in Figure 2, there are three main submodels in a friction welding model: a process model, a transient thermal model, and a microstructure evolution model. In friction welding of some alloys such as steels, the material at the weld interface will be heated and a significant amount of grain growth may occur. If such grain growth is known

---

T.C. NGUYEN, formerly Postgraduate Student, with the Department of Mechanical Engineering, University of Waterloo, Waterloo, ON N2L 3G1 Canada, is now Professor with the School of Engineering and Information Technology, Conestoga College, Kitchener, ON N2G 4M4 Canada. Contact e-mail: tnguyen@conestogac.on.ca D.C. WECKMAN, Professor, is with the Department of Mechanical Engineering, University of Waterloo, Waterloo, ON N2L 3G1 Canada. Contact e-mail: dweckman@uwaterloo.ca

Manuscript submitted August 10, 2005.

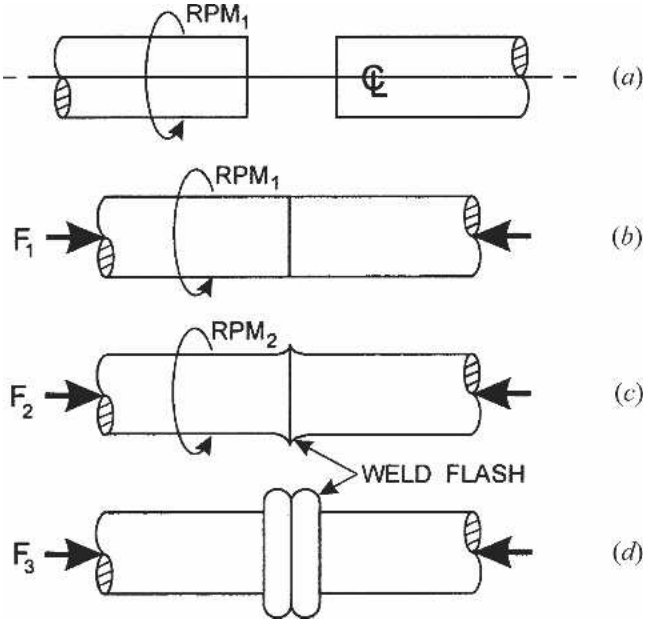

Fig. 1—The four stages of direct-drive friction welding: (*a*) start-up stage, (*b*) heat-up stage, (*c*) burn-off stage, and (*d*) forging stage.

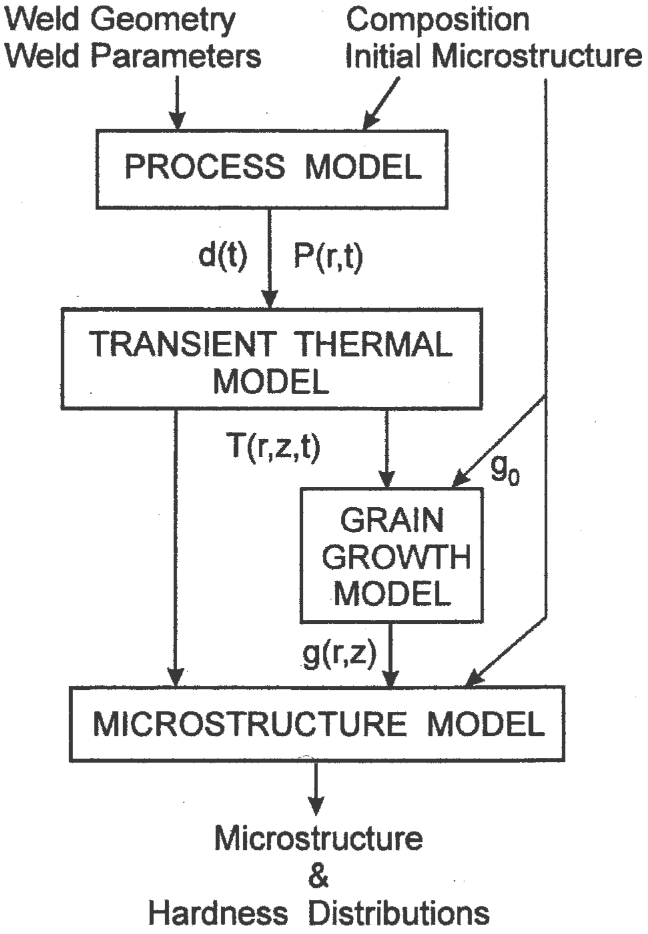

Fig. 2—An overall model of friction welding consists of a process model, a transient thermal model, a grain growth model, and a microstructure evolution model.

to influence the rate of subsequent solid-state transformations, then a grain growth model as shown in Figure 2 is also required.

During friction welding, heat is generated at the weld interface by a combination of friction between the two faying surfaces during the heat-up stage and plastic deformation that takes place at the interface during the burn-off stage. A friction welding process model must predict the effects of the process parameters, the component geometry, the chemical composition of the base metals, and the initial microstructure on the power generated at the weld interface, $P(r,t)$, as well as the relative axial displacement of the parts, $d(t)$, that normally takes place during the burn-off stage of the friction welding process.

Different models of the power generated at the weld interface during friction welding have been proposed. These include the constant power input models by Vill[2] and Bendzsak and North[3] as well as more detailed process models by Rykalin *et al.*[4] and Potapov *et al.*[5] The latter process models were developed to predict the input power as a function of the process parameters, an assumed constant coefficient of friction between the two weld specimens, the specimen geometry, and the material. The coefficient of friction is an empirical parameter that must be determined experimentally. The input power predicted by these simple models is by definition constant during the heat-up and burn-off stages. However, experimental measurements of power required during these stages of friction welding have been found to vary significantly with time during a friction weld.[2]

In the absence of a comprehensive process model, a number of different approaches have been used to model the power and heat generated at the interface during a friction weld. For example, Rich and Roberts[6] employed a number of empirical equations based on experimentally measured power data. Bendzsak and North[3] assumed an average power density evenly distributed within a narrow region at the weld interface. Finally, Cheng[7] used measured power data directly to define $P(t)$ in his numerical thermal model of friction welding.

As indicated in Figure 2, the transient thermal model uses the time varying power generated during welding, $P(r,t)$, to define the boundary condition at the weld interface. The thermal model is used to predict the time-temperature history, $T(r,z,t)$, of the metal during and after the friction welding process. Various analytical[3,4,6,8] and numerical transient heat conduction models[7,9] have been proposed to simulate the time-temperature history within the HAZ of a friction weld. While analytical models are relatively easy to implement, numerical transient models are better able to incorporate more realistic boundary conditions, temperature-dependent thermophysical material properties, two-dimensional heat transfer, and a greater degree of geometric flexibility; *i.e.*, they can be used to model bar-to-bar, tube-to-tube, and bar-to-tube geometries.

As shown in Figure 2, the predicted time-temperature history, the material composition, the initial microstructure, and the austenite grain size are then used by the microstructure evolution model to determine the postweld microconstituents and the hardness distribution across the weld interface. To date, most microstructure evolution models for steel come from research aimed at predicting the residual stress, the resulting hardness, or the depth of the hardness layer during heat treatment of steel. Among these, three models, the Cruesot–Loire[10,11,12] model, Easterling *et al.*'s[13,14] model, and Kirkaldy *et al.*'s[15,16,17] model, have been shown to provide accurate predictions when compared to experimental data. The first two models were developed based on statistical analysis of continuous cooling transformation (CCT) diagrams. In addition, Easterling *et al.*'s[13,14] microstructure model includes the influence of austenite grain size on the decomposition of austenite to ferrite, pearlite, bainite, and martensite. However, these two models can only be used for certain steel compositions.[13,14] On the other hand, Kirkaldy *et al.*'s[15,16,17] microstructure evolution model was more comprehensive since it was based on consideration of the fundamental thermodynamic and kinetic principles of solid-state phase transformations. All three aforementioned microstructure evolution models can be adapted to predict the transformation and the evolution of various microstructures in the HAZ of a weld during and after friction welding.

The objective of the work reported here was to develop a transient thermal model and a microstructure evolution model of the direct-drive friction welding process.[18] These models could be used to predict the time-temperature history within the HAZ of plain carbon steel bars during friction welding as well as the distributions of volume fraction of the final microconstituents and hardness across the weld interface. To validate the accuracy of the models, all predictions were compared to experimentally measured data.

II. EXPERIMENTAL APPARATUS AND PROCEDURES

To obtain the power and the axial displacement data for the process model as well as to provide experimental data for validation of the transient thermal model and the microstructure evolution model, a number of direct-drive friction welding experiments were performed. A New Britain Thompson 15 kW (20 hp) direct-drive friction welder equipped with a programmable logic control (PLC) system was used in this study. The weld specimens were 19-mm-(3/4-in.)-diameter AISI/SAE 1045 hot-rolled steel bars with the composition listed in Table I. A PC-microcomputer–based data acquisition system was designed and built to monitor and record axial displacement of the parts, axial force, spindle speed, spindle torque, and power generated at the weld interface during welding.[18] Figure 3 shows the typical variation of the spindle speed and the axial compressive force during the heat-up, burn-off, and forging stages. The magnitude and duration of the rotational speeds (RPM_1 and RPM_2) and the axial forces (F_1, F_2, and F_3) during each stage of the weld must be specified in the PLC controller of the friction welder prior to welding. As shown in Figure 3, the resultant torque required and the axial displacement of the specimens vary in a nonlinear fashion during different stages of direct-drive friction welding. From the measured data, the welding power can be calculated by multiplying the rotational speed and the resultant torque at any given time. Clearly, the power generated at the weld interface also varies nonlinearly during a friction weld.

Table I. The Composition (Weight Percent) of the AISI/SAE 1045 Hot-Rolled Steel Bar

C	Mn	Si	S	P
0.47	0.67	0.23	0.02	0.009

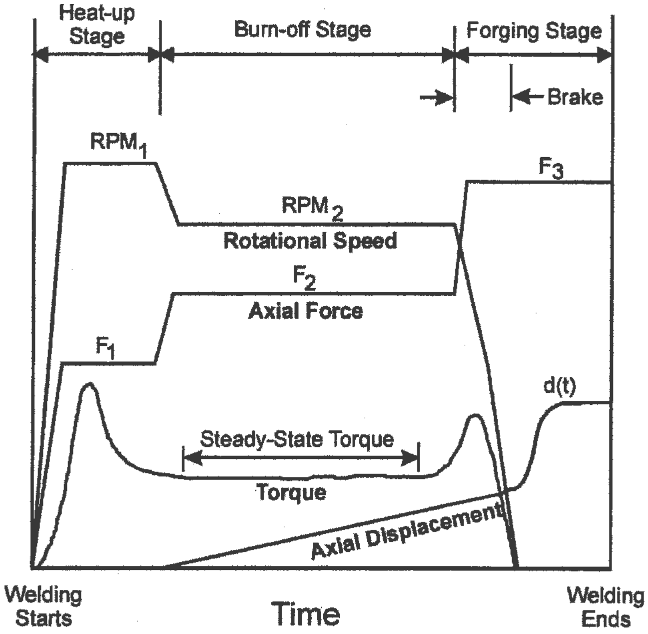

Fig. 3—The normal variations of the predefined rotational speeds and axial forces and the resultant torque and axial displacement during direct-drive friction welding.

Table II. The Weld Parameters Used for the Optimal, Long-Time, and Hard and Fast Welding Conditions

	Welding Conditions		
Welding Parameters	1 Optimal	2 Long-Time	3 Hard and Fast
Heat-up stage (s)	1	1	1
Burn-off stage (s)	2.5	12	2
Forging stage (s)	5	5	4
F_1, F_2 (kN)	8.9	8.9	35.3
F_3 (kN)	17.8	17.8	60.9
RPM_1, RPM_2 (rpm)	1000	1000	1800

To validate the results from the model, three significantly different sets of welding conditions were selected to produce welds with different HAZ dimensions and microstructures within the HAZ (Table II). In the optimal welding condition or welding condition 1, all parameters were set at their recommended optimal value.[19] In the long-time welding condition or welding condition 2, the heating time, (*i.e.*, the duration of the heat-up and burn-off stages) was prolonged to increase the maximum temperature at the weld interface, to increase the time for axial conduction of heat into the two work pieces, and to decrease the subsequent cooling rate. Finally, the hard and fast welding condition or welding condition 3 had a high rate of heat generation and high burn-off rate in a relatively short period of time. This was accomplished by using a short heating time in combination with high axial forces and rotational speeds. These three different welding conditions were expected to result

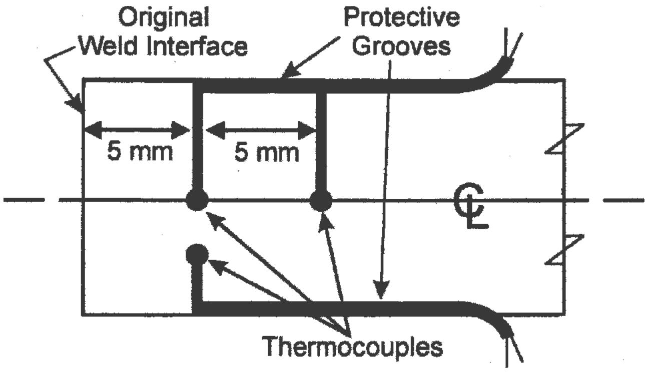

Fig. 4—Schematic of the stationary weld specimen showing the locations of the three thermocouples and their protective longitudinal grooves.

in significantly different cooling rates, microstructures, and HAZ widths that should be predicted by the model. Acceptable welds were produced with all three welding conditions.

Three type-K (chromel-alumel) thermocouples with 0.813-mm- (0.032-in.)-diameter stainless steel sheaths were used to measure the temperature within the stationary specimen during and after welding. Their locations within the stationary specimen are shown in Figure 4. To protect the thermocouples from being crushed by the flash during welding, the thermocouples were embedded in longitudinal grooves cut along the outer surface of the specimen. After welding, the specimens were cut in the longitudinal direction, mounted, and etched using a 4 pct Nital solution.[20]

III. MODEL DESCRIPTION

A. *Process Model*

In friction welding, the rubbing action between the two weld interfaces during the heat-up stage and the subsequent plastic deformation that takes place at the interface during the burn-off stage generate heat at the weld interface. The combined effects of this heat and the plastic deformation are ultimately responsible for the formation of the solid-state bond between the two components. As shown in Figure 2, the distribution and the amount of heat generated at the interface, $P(r,t)$, and the axial displacement of the specimens, $d(t)$, due to the plastic deformation and flash formation during welding depend on the process parameters used, the specimen geometry, and the material composition. Because a comprehensive process model does not yet exist, in this study, the power and the axial displacement were measured during welding using the PC-microcomputer–based data acquisition system. This is similar to the approach used previously by Cheng.[7] The measured power (torque × rotation speed) was used in the transient thermal model to define an assumed uniformly distributed heat flux boundary condition at the weld interface during the initial heating stage of welding. Meanwhile, the measured axial displacement data were used to incorporate the effects of the axial displacement of the material toward the weld interface during welding on the predicted transient temperature, microstructures, and HAZ size. This was also required in order to facilitate direct comparison between the temperatures measured by the embedded thermocouples and the temperatures predicted by the transient thermal model.

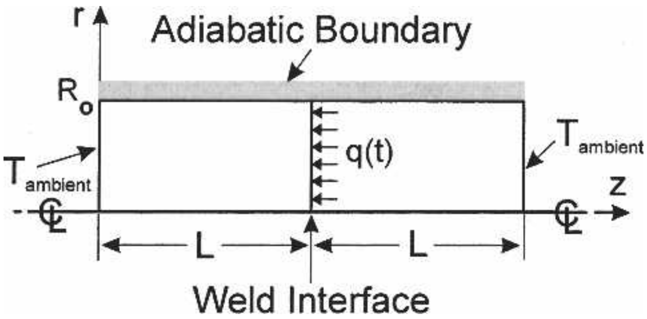

Fig. 5—The geometric domain and the boundary conditions used in the transient thermal model.

B. *Transient Thermal Model*

In the friction welding thermal model, the heat was assumed to be generated by frictional work and the plastic deformation that takes place at the two faying surfaces. This heat is conducted from the weld interface in the axial direction to the rest of the specimens. Figure 5 is a schematic diagram showing the domain and the boundary conditions used in the thermal model. The weld specimens were initially assumed to be at room temperature. The lateral surface of the specimen was assumed to have an adiabatic boundary condition, since heat lost by convection and radiation has been previously shown by Cheng[7] to be negligible. As illustrated in Figure 5, the length of the modeled specimens, L, was selected such that the ends remained at the ambient temperature, T_{ambient}, throughout the duration of the simulation period. Since the problem was assumed to be two-dimensional, axisymmetric and transient, the general form of the governing energy equation is:[21]

$$\frac{1}{r}\frac{\partial}{\partial r}\left(k(T)r\frac{\partial T}{\partial r}\right)+\frac{\partial}{\partial z}\left(k(T)\frac{\partial T}{\partial z}\right)=\rho(T)c_p(T)\left(\frac{\partial T}{\partial t}\right) \qquad [1]$$

where r is the radial coordinate; z is the longitudinal coordinate; T is temperature; k(T) is thermal conductivity; $\rho(T)$ is material density; $c_p(T)$ is specific heat and t is time. The thermophysical material properties of AISI/SAE 1045 steel used in Eq. [1] were considered to be temperature dependent. However, the overall objective of this project was to run the numerical model on a personal microcomputer. The use of temperature dependent properties in the transient numerical thermal model increases the simulation time of the model to unacceptable levels. Thus, a number of compromises were made to properly account for the temperature dependent thermal properties while keeping the execution time of the model within an acceptable time frame.

A constant average value of 7,844 kg/m^3 was used for the density since the density of AISI/SAE 1045 steel has a relatively weak temperature dependence over a wide temperature range.[22] Pehlke *et al.*[22] provide temperature dependent thermal conductivities for 1026 and 1086 steels. However, in this study, a constant value of thermal conductivity was used. This value was based on an integrated average value of the thermal conductivity over the temperature range from room temperature to 1673 K. For 1026 and 1086 steels, the integrated average values of the thermal conductivity were calculated to be 35.6 W/m · K and 34.0 W/m · K, respectively. Based on the weight percentage of carbon, linear interpolation between these values gave the average thermal conductivity of 35 W/m · K for AISI/SAE 1045 steel.

Watt *et al.*[23] curve-fitted existing experimentally measured specific heat for plain carbon steel into two equations. For temperatures less than 1000 K, the specific heat, $c_p(T)$ (J/kg · K), is given in terms of absolute temperature (K) by:

$$c_p(T) = \frac{1.117 \times 10^6}{(1010 - T)^2} + \frac{12622}{1010 - T} + 0.3485 \times T + 355.6 \qquad [2]$$

and for temperatures greater than 1000 K by:

$$c_p(T) = \frac{1.225 \times 10^8}{(T - 990)^4} + 0.1381 \times T + 585.7 \qquad [3]$$

In the present study, an integral average value of the specific heat between room temperature and 1673 K was used in the transient thermal model during the welding phase. This calculated average specific heat, 821.7 J/kg · K, was determined using a similar method as described for the thermal conductivity. To improve the temperature prediction during the cooling stage, however, a new value of specific heat was used. This was based on an integrated average value of the specific heat between 773 K (500 °C) and the temperature at each specific location within the domain at the beginning of the cooling stage. If the peak temperature at a specific location was less than 773 K, the specific heat was assigned a value determined by Eq. [2]. This scheme provided a better estimate of the actual temperature dependent specific heat while still using a constant value for computational efficiency.

At the weld interface, the experimentally measured power data was used to define a heat flux boundary condition. Following Cheng,[7] in the absence of a comprehensive process model, this heat flux was assumed to be distributed uniformly over the interface; thus, the heat flux, q(t), as shown in Figure 5, was calculated using the measured power divided by the cross-sectional area of the specimen. While it is recognized these boundary conditions will reduce the transient thermal model to a one-dimensional transient model, *i.e.*, there will be no radial variation in temperatures and the first term in Eq. [1] will be negligible, in the present study, the transient thermal model was formulated as a two-dimensional model so that it might also be used to model two-dimensional problems such as tube-to-bar friction welds.

When the measured power data is used for the entire duration of the heating period, the predicted temperatures at the weld interface have been found by Midling and Grong[8] to increase beyond the melting point of the metal. This does not occur in actual welds, because a dynamic balance is reached between the rate of heat generated at the interface and the heat lost by conduction in the axial direction plus the sensible heat contained in the metal that is carried away from the interface as the flash.[8] To prevent this unbounded temperature increase in the thermal model, Midling and Grong[8] switched from a constant flux boundary condition to a constant temperature boundary condition at the weld interface when the average predicted temperature on the welding surface exceeded a specified maximum temperature, T_{max}. This technique was also used in the present study where T_{max} was manually assigned a value between 70 to 90 pct of the melting point of AISI/SAE 1045 steel (*i.e.*, $1171 \text{ K} \leq T_{max} \leq 1506 \text{ K}$).[9] At the end of the burn-off stage, the heating period was over and the weld interface was assumed to be adiabatic, thus allowing the weld to cool down.

During the burn-off stage of a friction weld, hot material at the weld interface is forced radially outward to form the flash while new material is constantly brought to the weld interface by the relative axial displacement of the two work pieces towards the weld interface during the burn-off stage. As a consequence, all embedded thermocouples were displaced towards the weld interface. To permit direct comparison between the measured and predicted temperatures, the effects of this relative motion must be incorporated into the model. Upon completion of the thermal simulation, the temperature data was post-processed to compensate for the axial displacement that normally took place using the measured displacement data, d(t). The axial displacement compensating scheme is required to approximate the effects of the axial displacement on the predicted temperatures. It is best described using the following example.

Initially, the location of interest was a nodal point in the numerical model located on the centerline and 5 mm from the original weld interface. This corresponds to the initial location of the thermocouple. After a short time period into the weld cycle, the measured displacement data, d(t), indicated the material and the thermocouple had been axially displaced by 0.25 mm toward the weld interface. Up to this time, the post-processing program had being selecting the temperature data at a location 5 mm from the weld interface as the time-temperature history of the location of interest. However, knowing that the material and the thermocouple had been axially displaced by 0.25 mm, the post-processing program then selects the temperature at the new location 4.75 mm from the weld interface. This process is continued until the end of the weld simulation. As a consequence, the final time-temperature history measured by an embedded thermocouple and predicted by the model consists of temperatures versus time at axial positions that vary with time relative to the weld interface during the weld.

The transient thermal model was formulated and solved on a personal microcomputer using the numerical finite element method. Details of the finite element method formulation can be found in standard texts such Huebner and Thornton.[24] In this work, the modeled domain was discretized using axisymmetric triangular ring elements. As shown in Figure 6, a sample

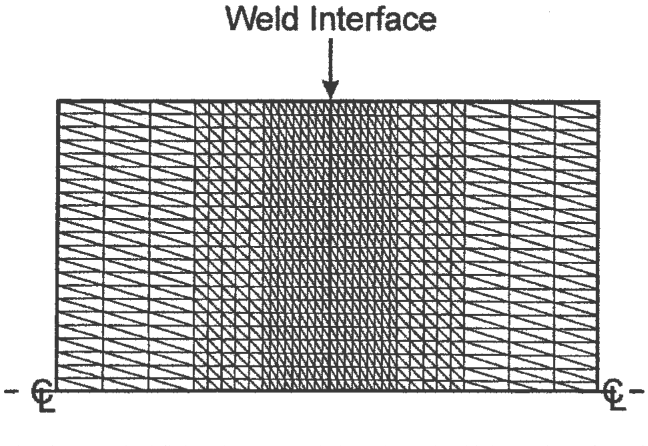

Fig. 6—A typical finite-element graded mesh used, which consists of 1496 triangular, toroidal elements.

graded mesh with 1,946 elements was used with small elements concentrated at the interface where high thermal gradients were expected. In the implementation of the transient thermal model, the Crank-Nicolson time-marching scheme was used to solve the time derivative of temperature since this particular time-marching method is unconditionally stable.[25] The thermal model utilized the Gauss-Seidel iterative solver to solve for the temperature field in the entire domain.[25]

Figure 7 details the program logic of the transient thermal model in a flowchart format. For convenience, the program logic of the transient thermal model was grouped into six major blocks of program execution. After mesh generation and initial finite element formulation, the model calculated the nodal temperatures of the domain during the heating stage based on the measured power data. Once the weld interface reached a maximum temperature, T_{max}, the program progressed to the equilibrium stage, in which the weld interface boundary condition was reformulated to a Dirichlet or constant temperature boundary condition, *i.e.*, $T = T_{max}$, in order to prevent unbounded temperature increase at the weld interface. When the welding cycle or equilibrium stage was completed, the program entered the cooling stage in which the interface boundary condition was changed to a Neumann boundary condition, *i.e.*, $q(t) = 0$, and the program continued to determine the nodal temperatures of the domain. At the end of the simulation, post-processing

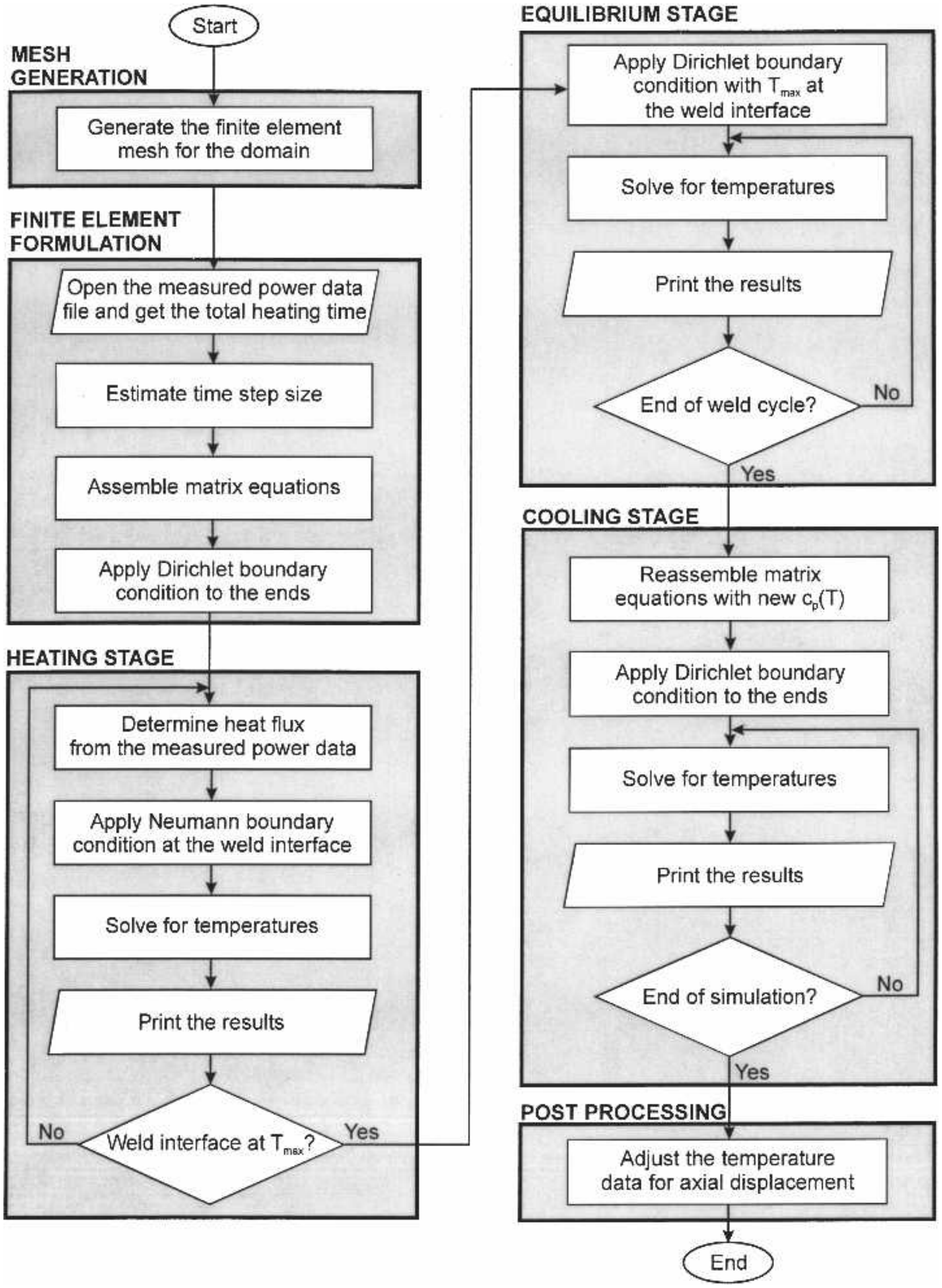

Fig. 7—Flowchart of the transient thermal model.

of the temperature data was performed to compensate for the axial movement of the material.

C. *Grain Growth Model*

During friction welding of steel, the high temperature experienced by the metal within the HAZ causes a transformation of the as-received microstructure to austenite. During the time spent as austenite, grain growth occurs. Since the austenite grain size is known to influence the rate of transformation of austenite to its various daughter products, a model of austenite grain growth is required.[13] In this study, the grain growth model originally proposed by Easterling and co-workers.[13,14] was implemented to calculate the austenite grain size prior to its decomposition. This model is given by the expression:

$$g^2 = g_o^2 + k_g \int_{t_1}^{t_2} \exp\left(\frac{-Q_g}{R \times T(t)}\right) dt \qquad [4]$$

where g is the final average austenite grain size (mm), g_o is the original austenite grain size (mm), k_g is the kinetic growth constant ($\text{mm}^2\,\text{s}^{-1}$), t_1 and t_2 are the time limits of the grain growth period, R is the universal gas constant (8.315×10^{-3} kJ/mol · K), Q_g is the activation energy for austenite grain growth (235.175 kJ/mol)[13] and T(t) is time varying temperature (K).

In the present study, the value of g_o and k_g for the AISI/SAE 1045 steel were experimentally determined to be 44 μm and $4.7 \times 10^4\ \text{mm}^2\,\text{s}^{-1}$, respectively. The start of the grain growth period, t_1, was defined to be the time when the steel is heated 50 K above the austenite transformation temperature. The end of the grain growth period, t_2, is the time when the temperature of the steel cools back to the austenite transformation temperature.

According to Eq. [4], the calculated austenite grain size, g, is in millimeters. However, the microstructure evolution model described in the next section uses the ASTM grain size number, G. Thus, the following non-linear regression relationship was used to convert the austenite grain size, g, in millimeters to the ASTM grain size number, G:[26]

$$G = -2.89 \times \log_{10}(g) - 2.95 \qquad [5]$$

D. *Microstructure Evolution and Microhardness Models*

Upon cooling from the austenitic region, the austenite phase begins to decompose into ferrite, pearlite, bainite and/or martensite upon reaching the respective transformation starting temperatures. In this study, the microstructure evolution model utilizes a series of empirical equations to predict the equilibrium transformation temperatures based on the steel composition. There are essentially four transformation temperatures: Ac_1 - the temperature at which pearlite starts to form, Ac_3 - the austenite-ferrite transformation temperature, BS - the temperature at which bainite starts to form and MS - the temperature at which martensite starts to form. The starting temperatures, Ac_1,[27] Ac_3,[27] BS,[17] and MS[28] are given by the following empirical equations:

$$\begin{aligned} Ac_1(°C) = {} & 723 - 10.7(\text{pct Mn}) - 16.9(\text{pct Ni}) + 29(\text{pct Si}) \\ & + 16.9(\text{pct Cr}) + 290(\text{pct As}) + 6.4(\text{pct W}) \end{aligned} \qquad [6]$$

$$\begin{aligned} Ac_3(°C) = {} & 910 - 203\sqrt{(\text{pct C})} - 15.2(\text{pct Ni}) \\ & + 44.7(\text{pct Si}) + 104(\text{pct V}) + 31.5(\text{pct Mo}) \\ & + 13.1(\text{pct W}) - 30(\text{pct Mn}) - 11(\text{pctCr}) \\ & - 20(\text{pctCu}) + 700(\text{pct P}) + 400(\text{pctAl}) \\ & + 120(\text{pct As}) + 400(\text{pct Ti}) \end{aligned} \qquad [7]$$

$$\begin{aligned} BS(°C) = {} & 656 - 58(\text{pct C}) - 35(\text{pct Mn}) - 75(\text{pct Si}) \\ & - 15(\text{pct Ni}) - 34(\text{pct Cr}) - 41(\text{pct Mo}) \end{aligned} \qquad [8]$$

$$\begin{aligned} MS(°C) = {} & 550 - 360(\text{pct C}) - 40(\text{pct Mn}) - 20(\text{pct Ni}) \\ & - 40(\text{pct Cr}) - 30(\text{pct Mo}) \end{aligned} \qquad [9]$$

where all alloying elements in the steel are expressed in weight percentage and the transformation starting temperatures are in Celsius (°C).

Kirkaldy *et al.*'s[15,16,17] microstructure evolution model was used to calculate the volume fraction of the microconstituents and the overall microhardness distributions across the heat affected zone of the friction weld based on the predicted time-temperature history at each numerical nodal point in the model. This microstructure evolution model has been used in previous studies to predict weld microstructures in the HAZ of welds made using other welding processes such as Gas Tungsten Arc and Gas Metal Arc welding.[23,29–31]

The development of Kirkaldy *et al.*'s[15,16,17] microstructure evolution model was based on consideration of the fundamental thermodynamic and kinetic principles of solid-state phase transformations. Essentially, the model consists of three differential equations which describe the decomposition rates of austenite to ferrite, pearlite and bainite, respectively. In Kirkaldy *et al.*'s[15,16,17] microstructure evolution model, the rate of decomposition of austenite to ferrite is described by the equation:

$$\frac{dF}{dt} = \frac{2^{(G-1)/2} \times \Delta T^3 \times F^{2(1-F)/3} \times (1-F)^{2F/3}}{[59.6(\text{pct Mn}) + 1.45(\text{pct Ni}) + 67.7(\text{pct Cr}) + 244(\text{pct Mo})] \times \exp\left(\dfrac{Q_f}{R \times T(t)}\right)} \qquad [10]$$

where F is the normalized volume fraction of ferrite; G is the ASTM austenite grain size number as defined in Eq. [5]; $\Delta T = (Ac_3 - T)$ is the ferrite undercooling; Q_f is the activation energy used in diffusion coefficient of carbon atoms during austenite to ferrite decomposition (96.278 kJ/mol)[23] and the remaining variables are the weight percentage of the various alloying elements in the steel.

Without normalization, the volume fraction as defined in Eq. [10] can be greater than unity. Clearly, this is unrealistic as the volume fraction of ferrite formed under equilibrium conditions depends on the composition according to the lever rule and is always less than 1. In Eq. [10], therefore, the volume fraction of ferrite is normalized by:[15,16,17]

$$F = \frac{X_F}{X_{FE}} \qquad [11]$$

where X_F is the total volume fraction of ferrite formed and X_{FE} is the maximum volume fraction of ferrite that can form at a specific temperature and composition under equilibrium conditions. Theoretically, F has an initial value of 0 and will be equal to 1 at equilibrium. Under non-equilibrium conditions, F will always be less than 1. When the temperature is below Ac_3 (Eq. [7]), but above Ac_1 (Eq. [6]), X_{FE} is calculated by using the lever law at that temperature.

In Kirkaldy *et al.*'s[15,16,17] microstructure evolution model, the rate of decomposition of austenite to pearlite is given by:

$$\frac{dP}{dt} = \frac{2^{(G-1)/2} \times \Delta T^3 \times P^{2(1-P)/3} \times (1-P)^{2P/3} \times D}{1.79 + 5.42[(\text{pct Cr}) + (\text{pct Mo}) + 4(\text{pct Mo})(\text{pct Ni})]} \quad [12]$$

where D is the effective diffusion coefficient of carbon atoms and defined as:

$$\frac{1}{D} = \frac{1}{\exp\left(\frac{-Q_{p1}}{R \times T(t)}\right)} + \frac{0.01(\text{pct C}) + 0.52(\text{pct Mo})}{\exp\left(\frac{-Q_{p2}}{R \times T(t)}\right)} \quad [13]$$

Here, P is the normalized volume fraction of pearlite; $\Delta T = (Ac_1 - T)$ is the pearlite undercooling and Q_{p1} (115.115 kJ/mol) is the activation energy for diffusion coefficient of carbon atoms in austenite. The diffusivity of carbon is affected by to the presence of other carbon atoms and alloying elements such as molybdenum. Thus, Q_{p2} (154.882 kJ/mol) is the activation energy in a modified diffusion coefficient which accounts for this interaction. This is required to calculate the effective diffusion coefficient of carbon atoms during the austenite-to-pearlite decomposition.[23] The remaining variables are the weight percentage of the different alloying elements in the steel.

In Eq. [12], the variable P is the volume fraction of pearlite normalized against the maximum amount of pearlite that could form at a specific temperature and composition under equilibrium conditions. At any given temperature, the maximum amount of pearlite that can form is equal to that of the untransformed austenite. The latter can be estimated by subtracting the equilibrium volume fraction of ferrite from one (*i.e.*, $1 - X_{FE}$). Therefore, the normalized volume fraction of pearlite in Eq. [12] is mathematically expressed as:[15,16,17]

$$P = \frac{X_P}{1 - X_{FE}} \quad [14]$$

where P is the normalized volume fraction of pearlite; X_P is the actual volume fraction of pearlite formed and X_{FE} is the maximum volume fraction of ferrite that can form under equilibrium conditions. Thus, $(1 - X_{FE})$ can be interpreted as the amount of untransformed austenite.

The rate of transformation of austenite to bainite can be described by the following equation:[15,16,17]

$$\frac{dB}{dt} = \frac{2^{(G-1)/2} \times \Delta T^2 \times B^{\frac{2(1-B)}{3}} \times (1-B)^{2B/3} \times \exp\left(\frac{-Q_b}{R \times T(t)}\right)}{[2.34 + 10.1(\text{pct C}) + 3.8(\text{pct Cr}) + 19(\text{pct Mo})] \times 10^{-4} \times f(B, C_{comp})} \quad [15]$$

where

$$f(B, C_{comp}) = \exp\{B^2 \times C_{comp}\} \quad [16]$$

and

$$C_{comp} = 1.9(\text{pct C}) + 2.5\,(\text{pct MN}) + 0.9(\text{pct Ni}) + 1.7(\text{pct Cr}) + 4(\text{pct Mo}) - 2.6 \quad [17]$$

where B is the normalized volume fraction of bainite; $\Delta T = (BS - T)$ is the bainite undercooling; Q_b is the activation energy in the diffusion coefficient of carbon atoms during the formation of bainite (115.115 kJ/mol)[23] and the remaining variables are the weight percentage of the various alloying elements in the steel.

As before, the normalization procedure for bainite is based on the ratio of the amount of bainite actually formed and the amount of untransformed austenite,[15,16,17] *i.e.*,

$$B = \frac{X_B}{X_A - X_F} \quad [18]$$

where X_B represents the actual amount of bainite formed; X_A is the volume fraction of austenite prior to decomposition and X_F is the actual amount of ferrite formed. Here, $(X_A - X_F)$ is used since the bainite reaction is a continuation of the pearlite reaction at lower temperatures.[23]

In Eq. [15], the function, $f(B, C_{comp})$, is a correction factor that was determined experimentally by Kirkaldy and Venugopalan[17] to facilitate correct prediction of the end of the bainite isothermal transformation time. This empirical function must be set to one whenever C_{comp} is negative. In Kirkaldy *et al.*'s[15,16,17] original microstructure evolution model, the correction function, $f(B, C_{comp})$, can be included in the decomposition rate equations for ferrite (Eq. [10]) and pearlite (Eq. [12]), respectively. However, in both cases, the correction function was set equal to one.[15,16,17]

Below the martensite starting temperature (*i.e.*, below MS, Eq. [9]), it was assumed that at this stage of the cooling and transformation, the cooling rate and the decomposition rate to martensite far exceeds the rate of the diffusion-based transformation to bainite. Therefore, below the martensite starting temperature, the remaining volume fraction of austenite was assumed to completely transform to martensite.

Since the hardness of the resultant microstructures is known to depend on the transformation temperature,[32] the following Vickers microhardness number (VHN) and temperature relationships were used in the present study:

For $T > 977K$, where only proeutectoid ferrite is produced,[13,14]

$$VHN = 150 \quad [19]$$

For $644K \leq T \leq 977K$, where ferrite, pearlite and bainite are produced, using curve fitting of the data taken from Reference [32],

$$VHN(T) = 60{,}100 - 288.7\,T + 0.521481\,T^2 - 4.17083 \times 10^{-4}\,T^3 + 1.2446 \times 10^{-7}\,T^4 \quad [20]$$

where VHN is the temperature dependent Vickers microhardness number and T is the transformation temperature in degrees Kelvin (K).

For $T < 644K$, where all remaining austenite is assumed to transform to martensite, from direct experimental measurement of the AISI/SAE 1045 steel used in this study:

$$\text{VHN} = 657 \qquad [21]$$

Using the above relationships, the overall Vickers microhardness number of a particular location within the HAZ is obtained using the following rule of mixtures:

$$\text{Overall Vickers Hardness Value} = \sum_{i=1}^{n} \text{VHN}(T) \times \Delta X_i(T) \qquad [22]$$

where ΔX_i is the total volume fraction of the microconstituents formed during an incremental time step, i, at transformation temperature T.

To calculate the volume fraction of each decomposition product, Eqs. [10], [12], and [15] must be integrated numerically due to their highly non-linear nature. In this study, an adaptive step-size controlled Runge-Kutta integration routine was used to solve the decomposition equations.[25] The execution logic for the microstructure evolution model is shown in Figure 8. In general, the program logic of the microstructure model was divided into heating and cooling stages. During the heating stage, the volume fraction of ferrite, pearlite and austenite were calculated based on the lever law. In this model, steel was assumed to completely transform to austenite once the temperature was 50 K into the austenitic region (*i.e.*, $T > Ac_3 + 50$).

In the cooling stage of the model, (see Figure 8) Eqs. [10], [12], and [15] were used to calculate the volume fractions of ferrite, pearlite and bainite, respectively. As illustrated in Figure 8, the decomposition of austenite to its daughter products begins when the steel cools down from the austenitic region and reaches the corresponding transformation temperatures. Ferrite will form when the steel cools down to

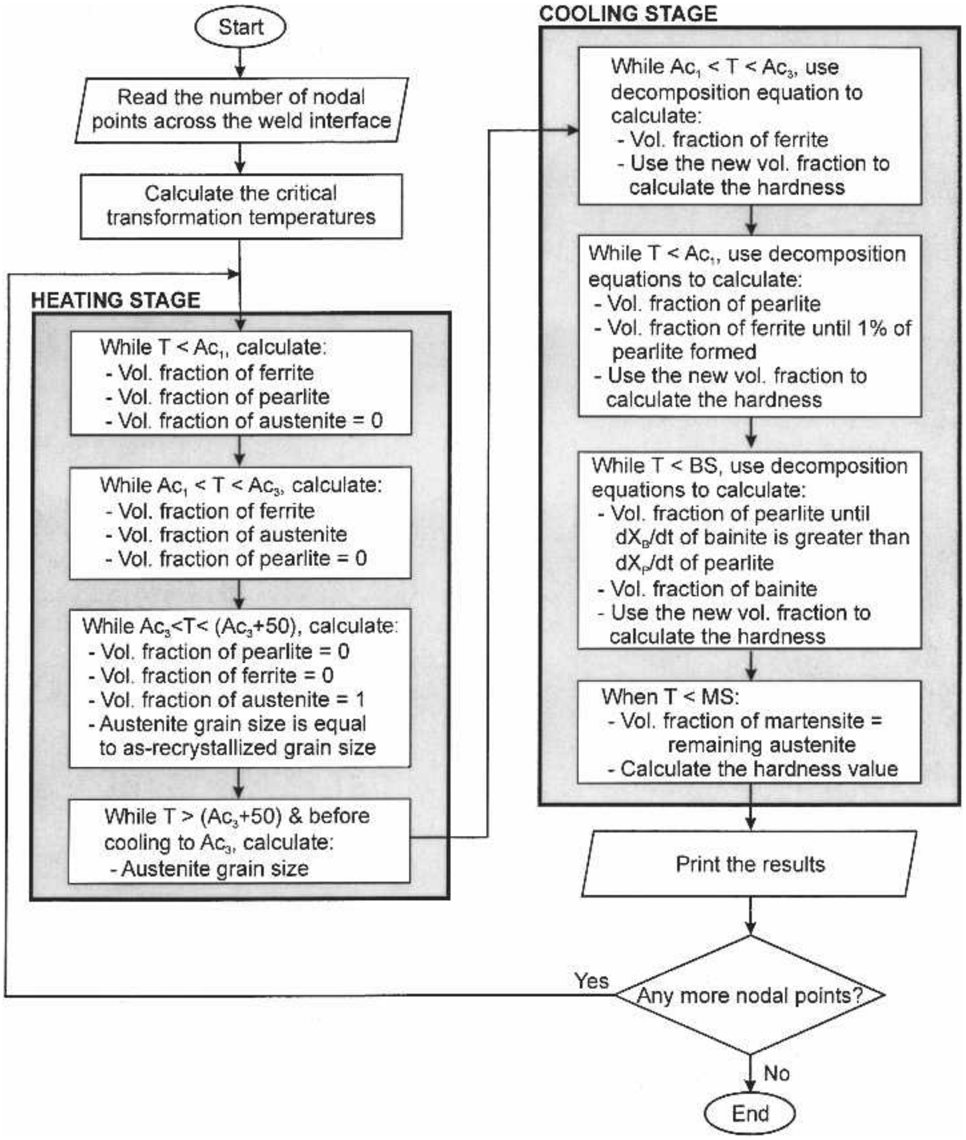

Fig. 8—Flowchart for the friction welding microstructure evolution model.

below the Ac_3 critical temperature. Below the pearlite transformation temperature (*i.e.*, below Ac_1), the austenite to ferrite transformation was assumed to stop when 1 pct volume fraction of pearlite was formed. Meanwhile, below the bainite starting temperature (*i.e.*, below BS), decomposition of austenite to bainite will occur. Since the bainite reaction is assumed to be a continuation of the pearlite reaction, decomposition of austenite to pearlite was assumed to stop when the rate of bainite formation was greater than the rate of pearlite formation (*i.e.*, dX_B/dt of bainite is greater than dX_P/dt pearlite). Finally, when the temperature was below the martensite starting temperature (*i.e.*, below MS), all remaining austenite was assumed to transform to martensite as indicated in Figure 8. At each time step increment, the newly calculated volume fraction was used to determine the overall hardness according to Eq. [21].

IV. RESULTS AND DISCUSSION

A. *Experimental Results for the Three Different Welding Conditions*

To validate the numerical model of direct-drive friction welding, friction welds were made using three different welding conditions. These were labeled as optimal, long-time and hard and fast welding conditions (see Table II). Figure 9 shows the measured axial displacement of the weld specimens when using each of the three welding conditions. Note that the axial displacement represents the movement of metal on one side of the weld interface only, *i.e.*, d(t)/2, and that time begins the instant the work pieces make contact. Initially, the displacement for both the optimal and the long-time welding conditions were similar, since both the axial force and rotational speed were the same (see Table II). For the first 1.8 s, there was no axial movement of either of the weld specimens, since this was the heat-up stage of the weld cycle. Following this, however, the metal at the interface begins to plastically deform and move radially outward under the influence of the axial force to form the flash. At the same time, the weld specimens moved towards the weld interface at a constant rate of displacement or burn-off rate. At approximately 3.5 s, the weld in the optimal welding condition entered the forging stage where there was a sudden increase in axial displacement rate. For this welding condition, the final axial displacement of one specimen was about 1 mm. Meanwhile, the long-time welding condition specimens continued to move towards the interface and each other and form more flash due to the longer heating time. At the end of the weld cycle, the final axial displacement for the long-time welding condition was about 4.5 mm.

The hard and fast welding condition specimens did not exhibit evidence of a heat-up stage. Rather, because the axial force was about 4 times greater than the previous two cases (see Table II), the flash began to form almost immediately after the weld specimens made contact and continued to form at a much higher burn-off rate than with the other two welding conditions. Within 3 s, the weld specimens had been displaced much further toward the weld interface than the other two welding conditions. In all three cases, these measured displacement data were used by the post-processing program to compensate for the axial movement of metal taking place during welding.

Figure 10 shows the measured power versus time for the welds made using the three different welding conditions. It is clear from the results shown here that the power generated at the weld interface is not constant, but depends strongly on the weld process parameters used and varies in a very non-linear manner during the welding process. The power required for the welds produced using the optimal and the long-time welding conditions gradually increased to a peak value of about 15 kW and then declined to an equilibrium value of about 7.5 kW. This steady-state power level is most

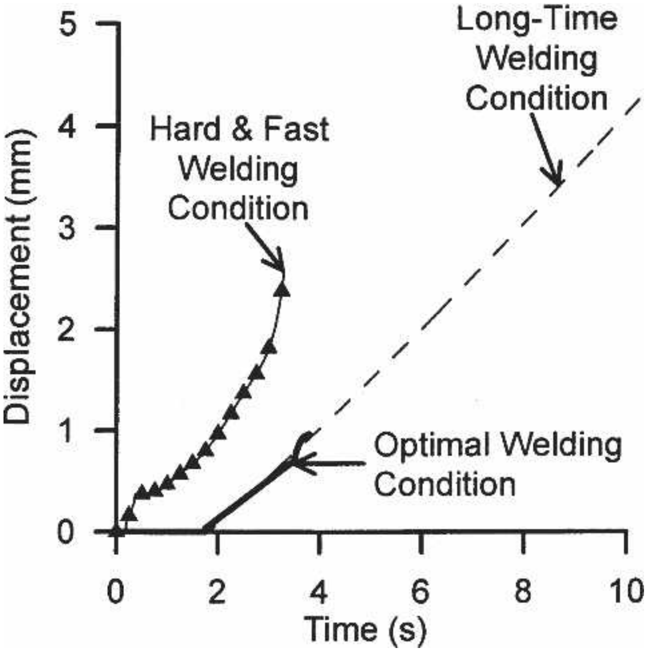

Fig. 9—Measured axial displacements of one specimen, *d*(*t*)/2, *vs* time for welds made using the three different welding conditions.

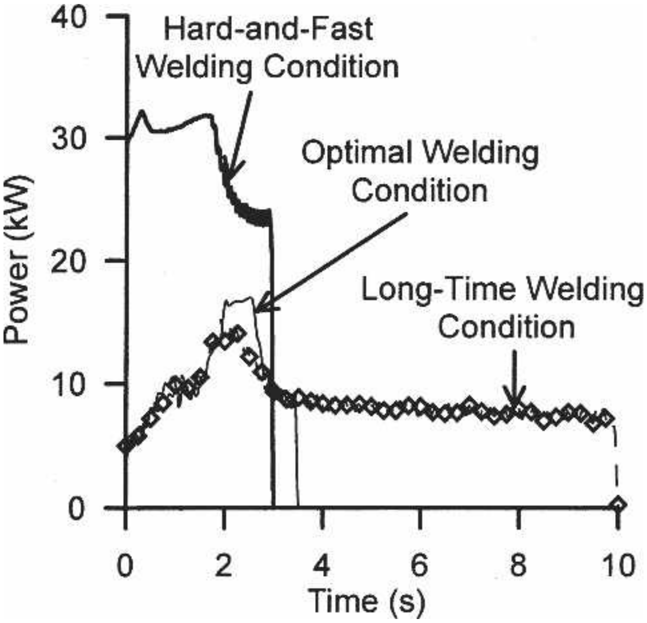

Fig. 10—Measured power *vs* time for welds made using the three different welding conditions.

apparent in the long-time welding condition. Meanwhile, the hard and fast welding condition generated much more power ($\approx$30 kW) at the weld interface during the 3 s welding time and appeared to approach a steady-state value of about 23 kW only at the end of the weld. These measured values of power were used as previously described to define the interface boundary condition of the transient thermal model.

Photomicrographs showing transverse sections of friction welds produced using the optimal, the long-time and the hard and fast welding conditions are shown in Figure 11. In all three cases, there is a slight hour-glass shape to the heat affected zone boundaries which suggests that the heat generated at the weld interface is not uniform, rather that it increases with increasing radial distance from the center of the weld specimens. However, there is currently no process model available that can be used to predict this radial variation in heat generation at the weld interface.

There are noticeable differences in the width of the heat affected zone and the amount of flash produced in the welds made using the three different sets of welding conditions. As expected, the weld made using the long-time welding condition has the most flash and widest HAZ (Figure 11(b)) as compared to welds made using the other two welding conditions. Also, there was so much plastic deformation and axial displacement that the thermocouple initially located 5 mm from the weld interface has moved into the zone of plastic deformation and been destroyed. The weld made using the hard and fast welding condition (Figure 11(c)) appears to have produced more flash than the weld made using the optimal welding condition (Figure 11(a)). Note that the thermocouple that was initially 10.0 mm from the weld interface has been displaced towards the interface and is now only 8.6 mm from the interface. Finally, the weld made using the optimal welding condition has a wider and more uniform HAZ than the weld made using the hard and fast condition.

B. *Compensating for Axial Displacement of the Weld Specimens*

In Figure 12, the predicted time-temperature history with and without compensation for the axial displacement of the weld specimen towards the weld interface during welding are plotted against the measured temperatures obtained from a thermocouple embedded at the centerline of a friction weld produced using the long-time welding condition. The measured temperature is seen to increase rapidly during welding to a peak temperature of about 1400 K. After the weld has been made, the rate of cooling is much slower. Without compensation for axial displacement of the thermocouple, the predicted rate of temperature increase during welding, the peak temperature and the cooling rate are all much less than the measured values. In fact, without compensation for axial displacement, the predicted peak temperature is 470 K less than the measured peak temperature. On the other hand, the predicted displacement-compensated time-temperature history shows excellent agreement with the measured data. Therefore, direct comparison between the predicted time-temperature history and that obtained experimentally from the embedded thermocouples is only possible provided that the effects of axial displacement of the weld specimen and the embedded thermocouple are incorporated properly in the model.

C. *Transient Thermal Model Predictions*

The predicted transient temperatures versus axial position for a weld produced using the optimal welding condition is shown in Figure 13. These predicted temperatures have been displacement compensated. Only the temperatures of the material located on the centerline and within 10 mm axial distance of the original weld interface were plotted. Since this is a friction weld of two 19 mm diameter 1045 steel bars, the temperature curves are symmetrical with respect

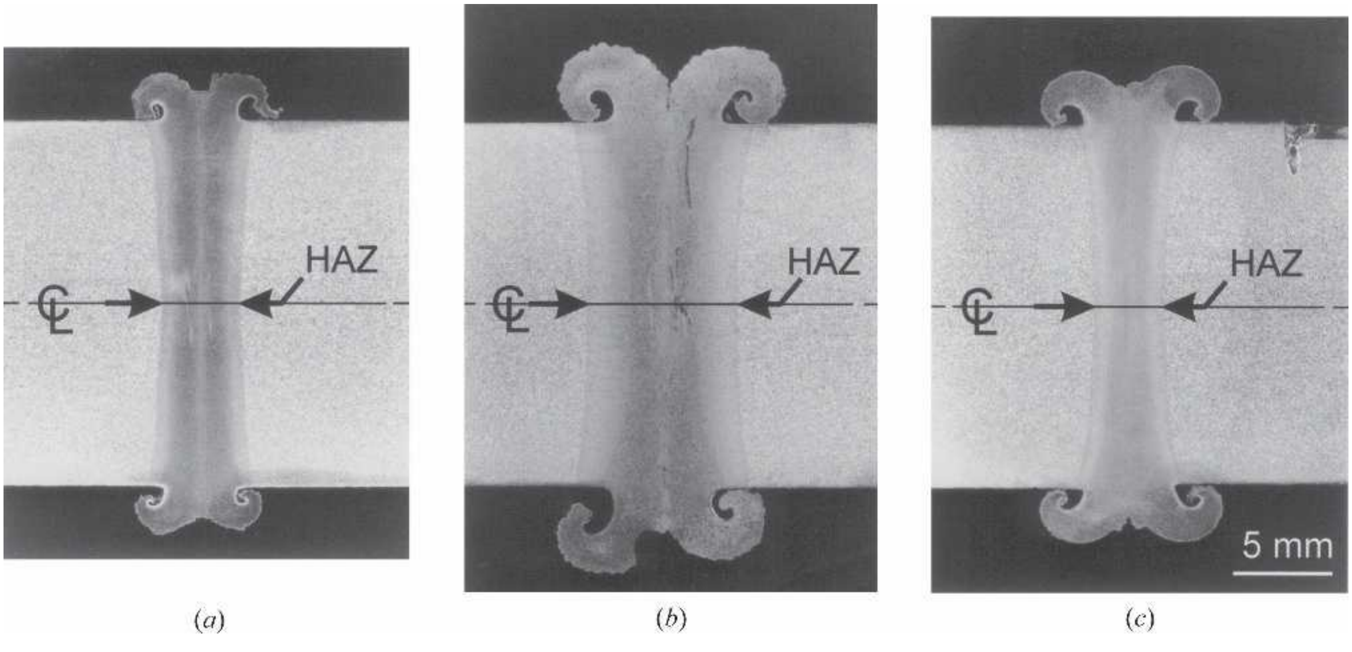

Fig. 11—Transverse sections of friction welds made between 19-mm-($\frac{3}{4}$-in.)-diameter AISI/SAE 1045 steel bars using (*a*) optimal, (*b*) long-time, and (*c*) hard and fast welding conditions.

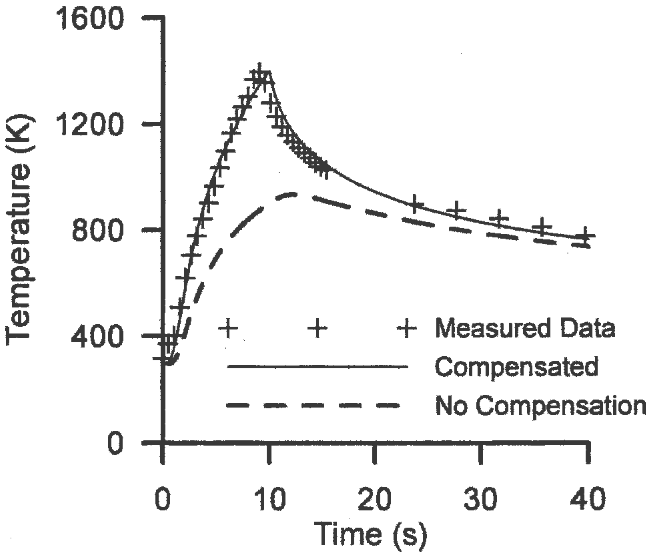

Fig. 12—The effect of compensating for the axial displacement of the weld specimen and thermocouple with respect to the weld interface on the measured and predicted temperatures *vs* time for the long-time welding condition.

to the weld interface. The predicted transient temperatures versus axial position for the welds produced using long-time and hard and fast welding conditions exhibited similar behavior to that shown in Figure 13.

A transient time-temperature simulation of a direct-drive friction weld begins with the application of the heat generated at the weld interface as a boundary condition. As shown, this heat generated at the weld interface causes the predicted temperature at the interface to increase rapidly. During the heating and burn-off periods, the slope of the time-temperature curve at the interface (0 mm axial position) is proportional to the heat input. This slope appeared to decline as the time increased beyond 2 s. This is consistent with the observed reduction in motor power during the latter portion of the burn-off stage (see Figure 10). In Figure 13(a), the width of the heat affected zone is defined by the material that is heated above the A_{c1} temperature of 989 K and therefore transforms into austenite. In this case, the heat affected zone is predicted to be about 4 mm. This is in very good agreement with that shown in the transverse section of the weld shown in Figure 11(a). After the interface reaches a temperature of $T = T_{max} = 1273$ K, the weld interface boundary condition was switched to a Dirichlet boundary condition with $T = T_{max}$. The interface temperature remained unchanged for the balance of the heating and burn-off periods. During the burn-off period, the heat can be seen to propagate further into the parent material thereby increasing the size of the heat affect zone.

After 3 seconds, the heating and burn-off stages were finished and the weld assembly entered the cooling period (see Figure 13(b)). On cooling, the heat was conducted away from the weld interface and lost to the surroundings through the ends of the weld specimens. The predicted rate of cooling is much slower than the rate of heating. Again, the temperature curves are symmetrical with respect to the weld interface.

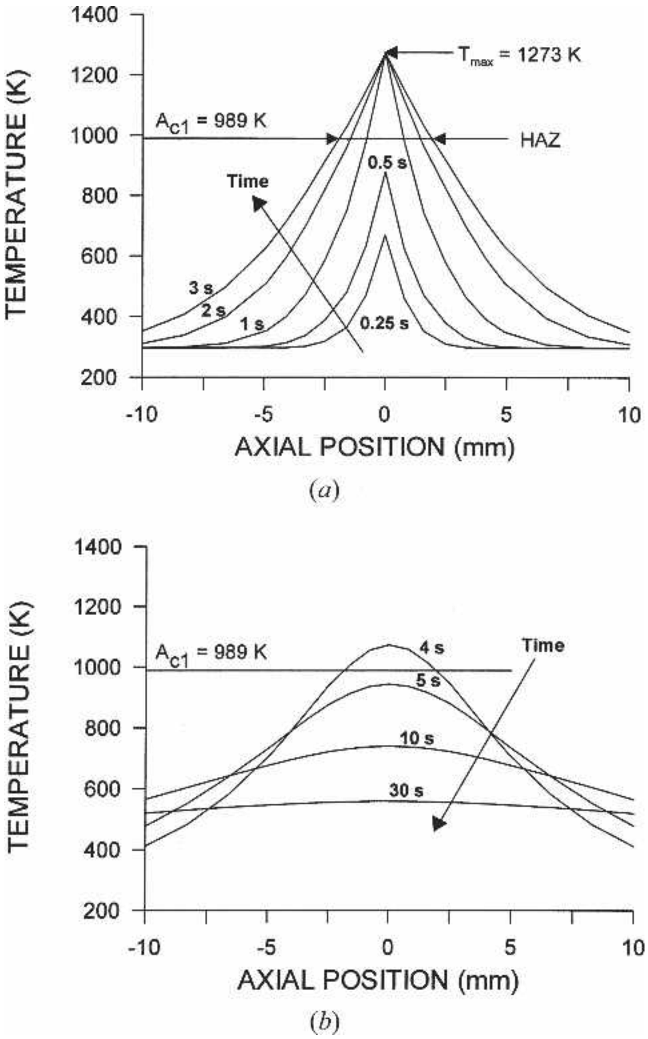

Fig. 13—Displacement-compensated predicted temperatures *vs* axial position along the center line of a weld made using the optimal welding conditions: (*a*) during the heating and burn-off stages and (*b*) during the forging and cooling stages.

Figure 14 shows the predicted and measured center line temperatures versus time for friction welds produced using (a) optimal, (b) long-time and (c) hard and fast welding conditions. The predicted temperatures (solid lines) are displacement compensated. These measured temperatures (data symbols) were those measured by the thermocouples located on the centerline of the stationary weld specimen and initially at a longitudinal distance of $z_o = 5$ mm and $z_o = 10$ mm, respectively, from the original weld interface. Because of the different welding conditions used, the amount of axial displacement toward the weld interface for the embedded thermocouples was different for each case. As a result, the final axial locations of the thermocouples and temperature profiles in Figure 14(a) are different than those in Figures 14(b) or (c). Thus, direct comparison between the heating and cooling rates shown in these three cases should not be made, because in each case, the thermocouple has moved a different amount and is at a different distance from the weld interface.

As indicated by all of the thermocouple measurements, the metal experienced a rapid rise in temperature to a peak value during welding. After the burn-off stage, the forging stage began and the metal gradually cooled down. Note that the gap in the measured results occurred while the data

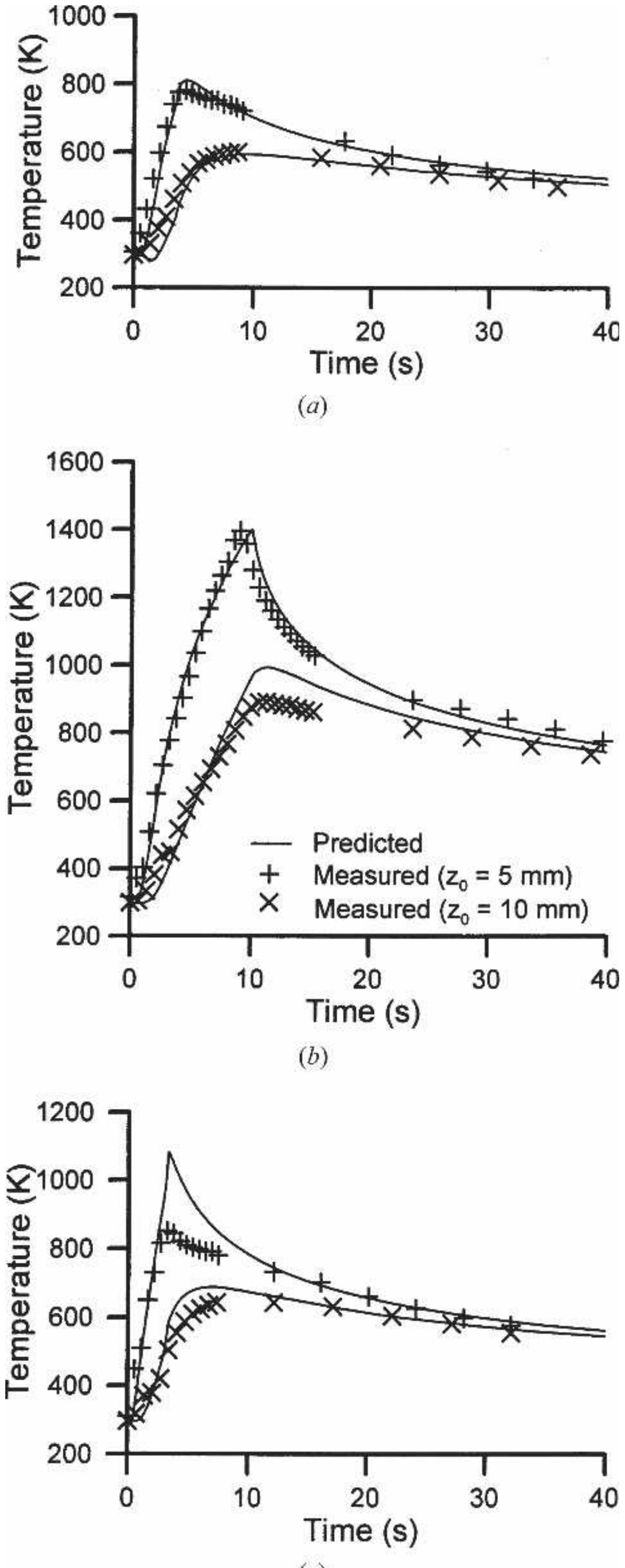

(*a*)

(*b*)

(*c*)

Fig. 14—The predicted and measured center line temperatures from embedded thermocouples originally placed at the center line and z_o = 5 mm and z_o = 10 mm from the weld interface of AISI/SAE 1045 steel friction welds made using (*a*) optimal, (*b*) long-time, and (*c*) hard and fast welding condition.

acquisition system was saving the measured data into a data file. Temperature measurements could not be made during this time period.

Overall, the predicted temperatures were in good agreement with the measured temperatures for all three welding conditions. For the optimal and the long-time welding conditions, the difference between the predicted and the observed temperatures and cooling rates were small. On the other hand, the difference was quite large for the friction weld produced with the hard and fast welding condition (see Figure 14(c)), especially for the thermocouple closest to the weld interface (z_o = 5 mm). In this case, the amount of flash formed around the weld interface was suspected to be a major factor affecting the peak temperature reached and the cooling rate. As indicated in Figures 9 and 10, the hard and fast welding condition had a short heating time, a high displacement rate and a high heat generation rate. Due to the high displacement rate, the heat generated at the weld interface was carried away from the interface quickly by the plastic deformation and stored as sensible heat in the flash. This rapid removal of the heated material would have prevented the interface temperature from increasing as much as was predicted by the numerical model. After welding, this sensible heat was conducted from the flash back into the HAZ of the weld thereby returning the sensible energy to the weld joint and reducing the cooling rate of the metal. Therefore, to facilitate accurate prediction of the measured cooling rates for this welding condition, an artificially large value of T_{max} was required in the thermal model.

For each welding condition, there was a maximum temperature, T_{max}, reached at the welding interface. To determine the actual value of T_{max} for a welding condition, several simulations were performed. The value of T_{max} was varied in each simulation and a comparison made between the measured and predicted temperatures. For example, in the optimal welding condition, when T_{max} was set at 1273 K, good correlation between the predicted and the measured temperatures was obtained. As T_{max} was increased beyond 1273 K, the predicted temperatures were much higher than the measured temperatures. On the other hand, when T_{max} had a value less than 1273 K, the predicted temperatures appeared to decrease much faster than observed from experimental measurement. Using this same procedure, T_{max} for the long-time and the hard and fast welding conditions were found to be 1483 K and 1453 K, respectively.

Experimental measurements by Squires[33] revealed that different maximum temperatures occurred at the weld interface depending on the welding conditions used. This trend was clearly evident in the predicted T_{max} values for the three different welding conditions used in the present study. While changing welding process conditions apparently affects the maximum temperature at the weld interface, the relationship between the welding parameters and the maximum temperature at the weld interface is not yet known. This must be part of future development of the process model.

For all three welding conditions, the value of T_{max} required for good correlation with measurements was much less than the melting temperature of AISI/SAE 1045 steel (~1670 K). This suggests that melting did not occur at the weld interface during friction welding of the steel bars. This is consistent with the results of Squires[33] and Tensi *et al.*[34]

D. *Calibration of the Microstructure Evolution Model*

Before using the microstructure evolution model, tests were performed to ensure that the austenite decomposition equations, Eqs. [10] through [18], could in the very least predict the Isothermal Transformation (IT) diagram of AISI/SAE 1045 steel.[32] The initial results, as shown in Figure 15, indicated that the decomposition equation of austenite to ferrite and that of austenite to bainite were able to predict the starting time for their respective transformations. The same, however, could not be said for the austenite to pearlite transformation. The long incubation time of the pearlite suggested that the undercooling term (*i.e.*, $\Delta T^3 = (Ac_1 - T)^3$) in the austenite to pearlite decomposition equation (Eq. [12]) did not have the proper effect and required adjustment. Initially, the undercooling term in the decomposition equation for austenite to pearlite had an exponent of 3. However, when the exponent of the undercooling term was set to 3.35, a reasonable starting curve for pearlite transformation was obtained as illustrated in Figure 16.

The predicted ending times for both the bainite and pearlite transformation were much shorter than experimentally measured values[32] (see Figure 15). In the decomposition equations, the correction function, $f(X, C_{comp})$, was originally proposed by Kirkaldy *et al.*[15,16,17] to retard the transformation rate such that the ending time of the reaction matched the experimental measurements. For example, in the austenite to bainite transformation, $f(B, C_{comp})$ was given by Eqs. [16] and [17]. Because the steel composition is constant, Eq. [16] varies only as a function of B during the transformation. Therefore, for the purposes of the present study, a new form of the correction function is proposed, *i.e.*,

$$f(X_i) = \exp(X_i^2 \times A) \qquad [23]$$

where X_i is the normalized volume fraction of either pearlite or bainite as before and A is a calibration constant. The value of A was varied until the predicted end of transformation time correlated with the measured time reported in the published IT diagram for AISI/SAE 1045 steel.[32] As seen in Figure 16, when the calibrated constant A was set to 2.5 and 1.5 in the bainite and pearlite decomposition equations, respectively, there was good correlation between measured IT data for AISI/SAE 1045 steel[32] and the predictions of Kirkaldy *et al.*'s[15,16,17] modified microstructure evolution model. Thus, using the above technique and an experimentally measured IT diagram, Kirkaldy *et al.*'s[15,16,17] microstructure evolution model can be calibrated for any steel composition.

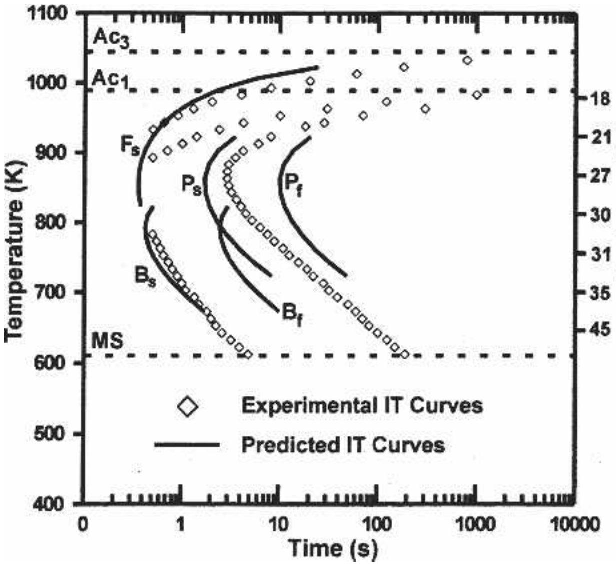

Fig. 15—Experimental IT curves for AISI/SAE 1045 steel[32] and transformation times predicted using Kirkaldy *et al.*'s[15,16,17] original microstructure evolution model.

E. *Microstructure Evolution Model Predictions*

In the as-received condition, the microstructure of the hot-rolled AISI/SAE 1045 steel bar consisted of ferrite and large pearlite colonies. As shown in Figure 17, the proeutectoid ferrite was situated at the prior austenite grain boundaries and surrounded the large pearlite colonies. The average microhardness for the as-received AISI/SAE 1045 steel was

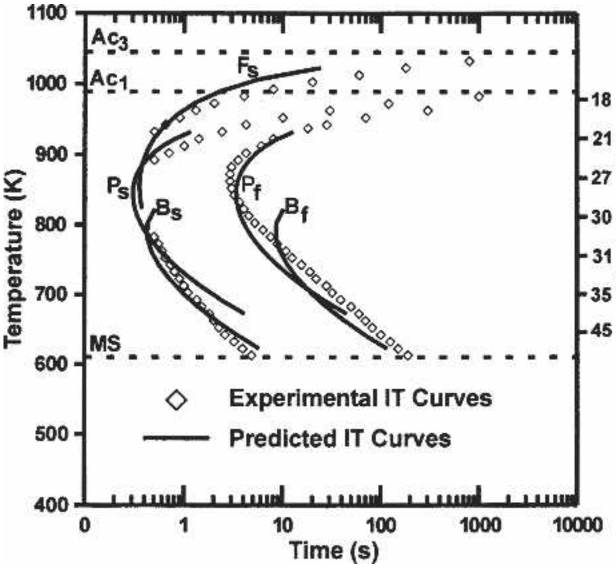

Fig. 16—Experimental IT curves for AISI/SAE 1045 steel[32] and transformation times predicted using Kirkaldy *et al.*'s[15,16,17] modified microstructure evolution model.

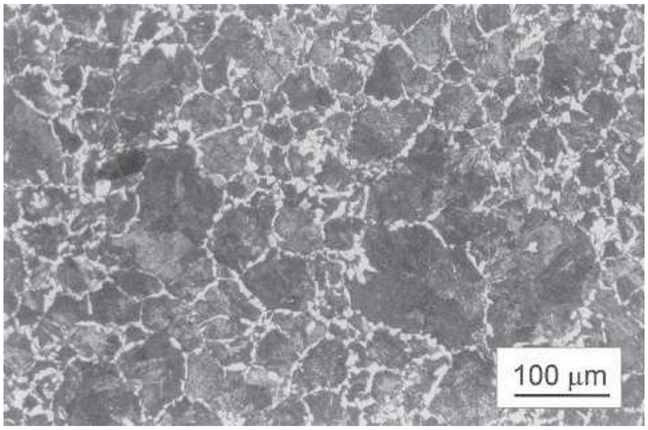

Fig. 17—The as-received microstructure of the hot-rolled AISI/SAE 1045 steel bar consisting of ferrite (white) decorating grain boundary and pearlite (gray) within the grains.

approximately 220 VHN which is higher than the measured VHN of the fully annealed AISI/SAE 1045 steel (181 VHN).

The predicted volume fractions of ferrite, pearlite and bainite, and martensite as a function of axial position in a friction weld made using the optimal welding condition is shown in Figure 18(a). Figure 18(b) is a photomicrograph taken on the centerline and at the weld interface of the same friction weld. From the plot, the predicted volume fraction of pearlite and bainite is seen to increase from 56 pct in the base metal to about 92 pct in the HAZ. There was about 7 pct volume fraction of martensite predicted in the HAZ. On the other hand, the volume fraction of ferrite decreases from 44 to about 0.8 pct. Comparison of these predictions with the photomicrograph of the microstructure in Figure 18(b) suggests that there is excellent qualitative agreement between the predicted and the observed microstructures. Similar results were also observed for welds made with the long-time (see Figure 19) and the hard and fast welding conditions (see Figure 20). Note that the volume fraction of ferrite in the weld made using the long-time welding condition was observed and correctly predicted to be greater than that in the other welds due to the slower cooling rate experienced by the HAZ of this weld (see Figure 19). Also, as would be expected, there was a significant decrease in the predicted volume fraction of martensite in this weld.

To further validate the results from the microstructure model, the area fraction of the resultant microstructures was measured for welds produced using different welding conditions. The measured area fraction of each microconstituent is a good indicator of the volume fraction of the post-weld microstructure.[20] The area fraction of each microconstituent was measured using a standard metallographic microscope with image analysis software. For simplicity, it was assumed

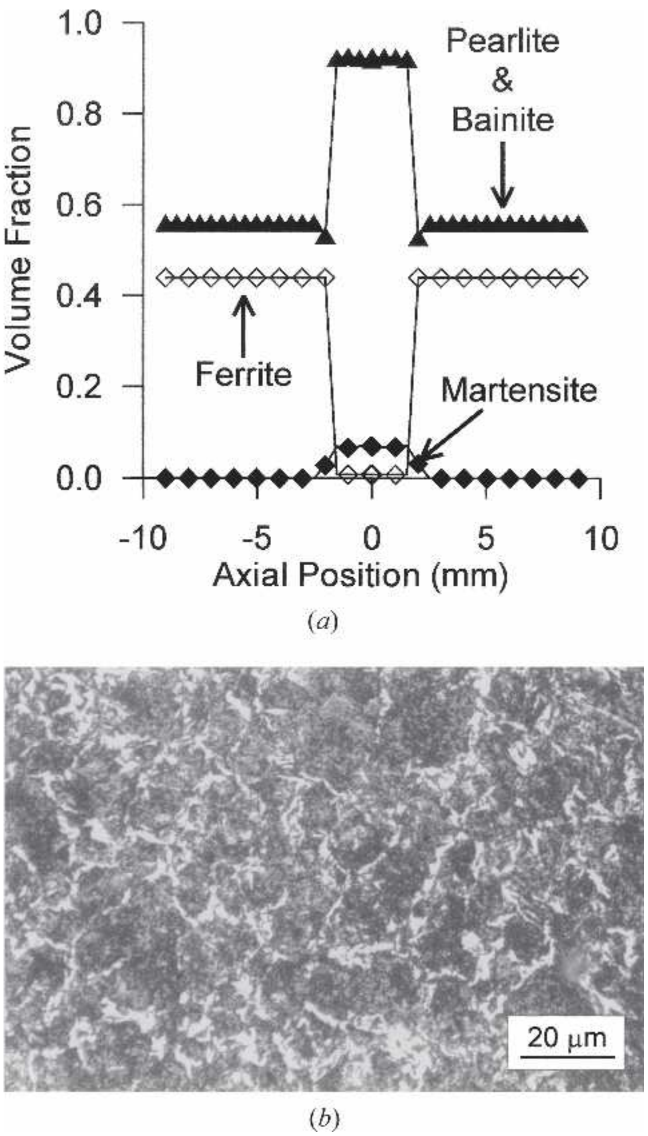

(*a*)

(*b*)

Fig. 18—Results of a friction weld made using the optimal welding condition: (*a*) predicted volume fraction of ferrite, martensite, pearlite, bainite; and (*b*) photomicrograph showing ferrite (white) and fine pearlite, bainite, and martensite (gray) at the weld interface and on the center line.

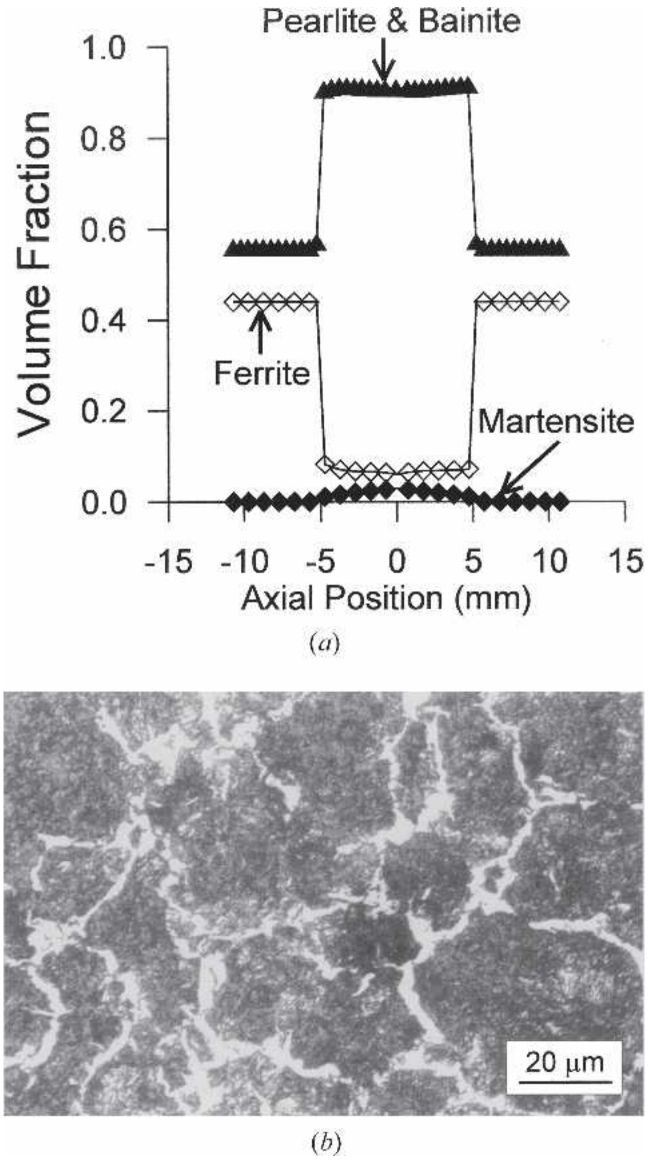

(*a*)

(*b*)

Fig. 19—Results of a friction weld made using the long-time welding condition: (*a*) predicted volume fractions of ferrite, pearlite, bainite, and martensite; and (*b*) photomicrograph showing ferrite (white) and fine pearlite, bainite, and martensite (gray) at the weld interface and on the center line.

that the darker gray phase is unresolvable fine pearlite and bainite while the white phase is either ferrite or martensite. For each welding condition, the measurement was taken at a position located on the centerline and at the weld interface. The measured area fractions are summarized along with the predicted volume fractions of the post-weld microstructure in Table III. As indicated, there was good agreement between the model predictions and the measured volume fractions of the resultant microconstituents in the friction welds produced using these different welding conditions.

The predicted and measured Vickers microhardness distribution versus axial position is plotted in Figure 21 for the friction welds produced using (a) the optimal, (b) the long-time and (c) the hard and fast welding conditions. In the weld produced using the optimal welding conditions, the measured microhardness increased from 220 VHN in the base metal to about 300 VHN within the HAZ of the weld. The model also predicted an increase in microhardness in the HAZ; however, the predicted values were between 10 and 25 VHN higher than the measured values (see Figure 21(a)).

The predicted and measured microhardness for the weld produced using the long-time welding conditions are shown in Figure 21(b). The microhardness in the HAZ of this weld increased to about 270 VHN which is less than the weld produced using the optimal welding conditions due to the slower cooling rates experienced by this weld and resultant higher volume fraction of ferrite and reduced volume fraction of martensite produced. Also, there was better correlation between the measured data and predicted microhardness values in the HAZ compared to the optimal welding condition. This may be due to the fact that the cooling rate and the peak temperature were well predicted by the transient thermal model (see Figure 14(b)).

The predicted and measured microhardness for the weld produced using the hard and fast welding conditions are shown in Figure 21(c). In this case, the microhardness in the HAZ increased to about 290 VHN and the model slightly over-predicted the microhardness. However, the correlation between the predicted and measured VHN was good considering the fact that a higher T_{max} was required in order to achieve the correct cooling rate.

The predicted microhardness distribution of each case shown in Figure 21 indicates the existence of a soft region between the unaffected metal and the HAZ and a very abrupt change in microstructure and microhardness at the boundary between the base metal and HAZ. This behavior was predicted, but not observed in the actual welds except possibly in the optimal weld shown in Figure 21(a). The temperature of the metal at this soft location peaked in the intercritical region or between the Ac_1 (990 K) and the Ac_3 (1018 K) temperatures. In this scenario, the microstructure evolution model predicted a larger volume fraction of austenite than the amount that probably actually formed. This was caused by the fact that in the model, an instantaneous microstructure transformation of the pearlite to austenite during the heating stage was assumed. As previously mentioned, the microhardness is a function of the transformation temperature. Since there was more austenite predicted to decompose to ferrite upon cooling than probably actually existed in this region of the weld, the predicted microhardness was lower than experimentally observed immediately adjacent to the base metal and higher than observed at the edge of the HAZ.

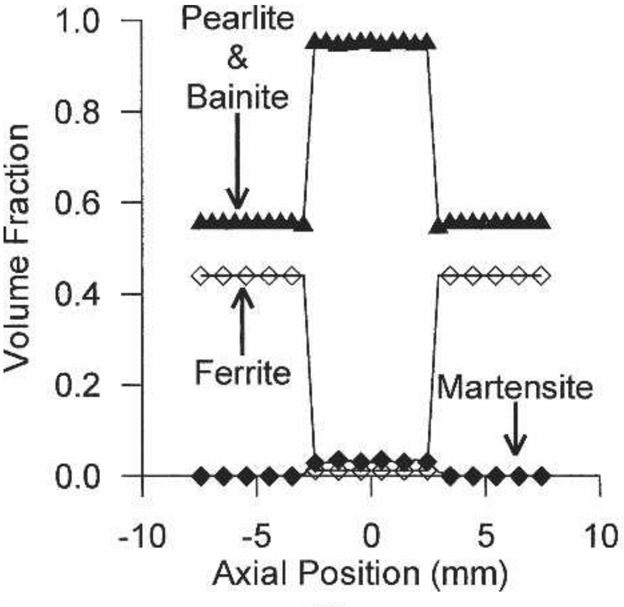

(*a*)

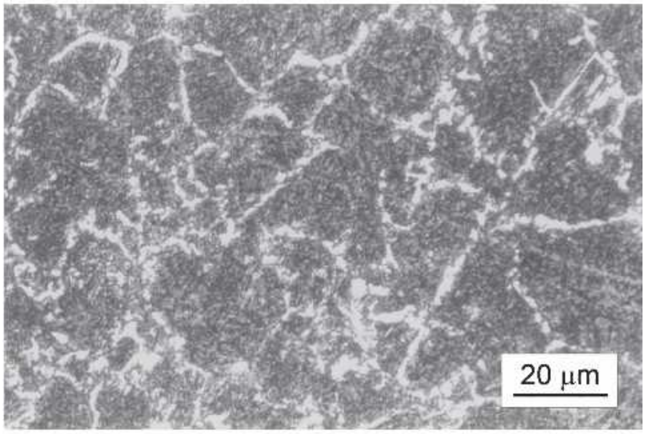

(*b*)

Fig. 20—Results of a friction weld made using the hard and fast welding condition: (*a*) predicted volume fractions of ferrite, pearlite, bainite, and martensite; and (*b*) photomicrograph showing ferrite (white) and fine pearlite, bainite, and martensite (gray) at the weld interface and on the center line.

Table III. The Predicted and Measured Percentage of the Resultant Microstructures for Friction Welds Produced Using the Optimal, the Long-Time, and the Hard and Fast Welding Conditions

	Optimal		Long-Time		Hard and Fast	
	Predicted	Measured	Predicted	Measured	Predicted	Measured
Pearlite and bainite	91.9 pct	91.2 pct	91.0 pct	89.5 pct	95.8 pct	96.3 pct
Ferrite and martensite	8.1 pct	8.8 pct	9.0 pct	10.5 pct	4.2 pct	3.7 pct

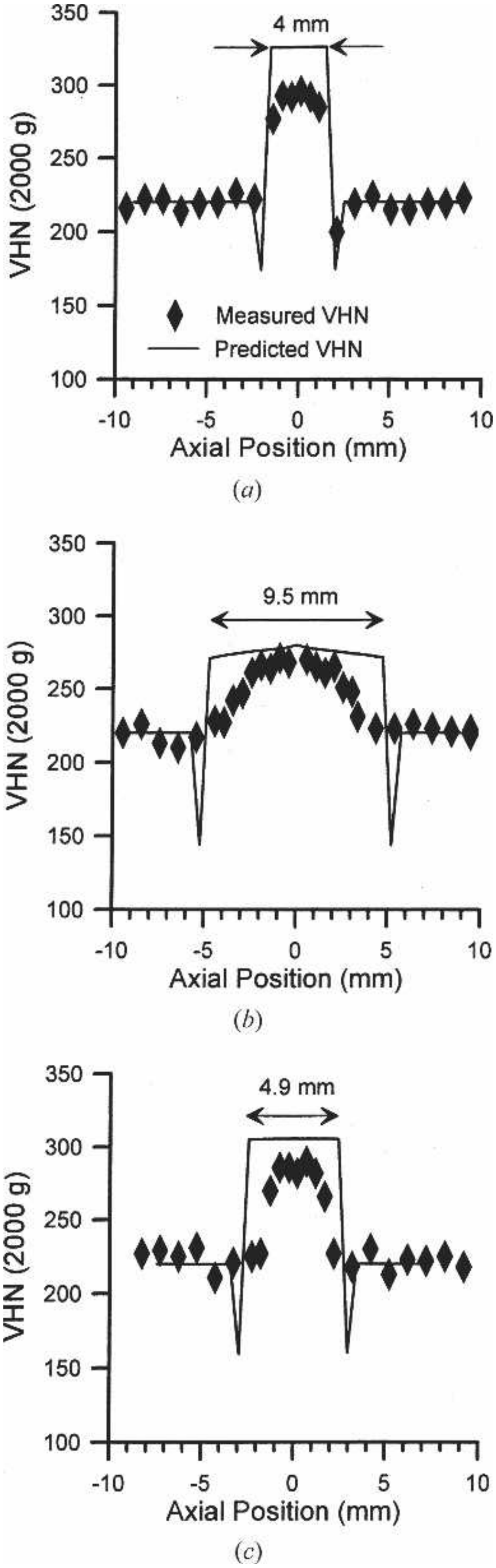

Fig. 21—The measured and predicted microhardness (VHN) *vs* axial position along the center line of welds made using (*a*) optimal, (*b*) long-time, and (*c*) hard and fast welding conditions.

Table IV. Measured HAZ Widths at the Centerline and Outside Diameter of Friction Welds Produced Using the Three Different Welding Conditions and the Predicted HAZ Widths

	HAZ Width (mm)		
	Measured		
Welding Condition	Center	Outside	Predicted
Optimal	4.0	5.8	4.0
Long-time	7.8	9.5	9.5
Hard and fast	3.5	5.7	4.9

To improve the microstructure and microhardness predictions for material that is heated only into the intercritical or low austenite temperature range, an austenite decomposition model is needed during the heating state. An austenite decomposition model would predict the effects of heating rate on the transformation kinetics of pearlite and ferrite to austenite. Using the austenite decomposition model, more accurate prediction of the volume fraction of austenite would be obtained during the heating cycle. This would lead to improved prediction of the resultant microconstituents and microhardness in the HAZ adjacent to the boundary between the base metal and HAZ.

The predicted width of the HAZ for the welds produced using the three different welding conditions are also indicated in Figure 21. The HAZ width predicted for the weld produced using the optimal welding conditions was 4 mm. This is in very good agreement with the HAZ width as evidenced by the microhardness measurements. As expected, the HAZ width of the weld produced using the long-time welding conditions was predicted to be almost twice as large (9.5 mm). This was due to the long burn-off time used during this weld which gave more time for heat to be conducted into the specimens. Finally, the HAZ width predicted for the weld produced using the hard and fast welding conditions was 4.9 mm, slightly larger than that in the weld produced using the optimal conditions. In the last two cases, the predicted HAZ widths appear to be slightly larger than the HAZ widths as evidenced by the microhardness measurements; however, in all cases, there is good qualitative agreement between the predicted and observed effects of the welding conditions on the HAZ widths.

As was previously noted in Figure 11, the HAZ in the welded specimens always had a slight hour-glass shape which suggests that the heat generated at the weld interface is not uniform, rather that it increases with increasing radial distance from the center of the weld specimens. The measured HAZ widths at the center line and outside diameter of friction welds produced using the optimal, long-time and hard and fast welding conditions and the predicted HAZ widths are shown in Table IV. The HAZ width of the weld produced using the optimal conditions, for example, varied from 4 mm at the centre to 5.8 mm at the outside edge adjacent to the flash (see Figure 11(a)) while the model predicted a 4 mm HAZ width which is the same as the observed center line width. While similar variations in the HAZ width were observed for the other two cases (see Figures 11(b) and (c)), as shown in Table IV, in all cases, the predicted HAZ was within the observed range of HAZ widths. Also, the model was able to correctly predict the qualitative effects of the welding conditions on the HAZ width, *i.e.*, the HAZ width of the long-time weld was larger than the optimal HAZ width and the hard and fast width was slightly larger than the optimal HAZ width.

At the present time, a comprehensive and rational process model that can predict the actual power distribution at the weld interface and the resultant slight hour-glass shape of the HAZ is not available. Thus, a constant power distribution assumption is a reasonable assumption until such time as a more comprehensive process model becomes available.

V. CONCLUSIONS

A model of direct-drive friction welding has been developed which can be used to predict the time-temperature histories, the resultant microstructure and the microhardness distribution across the weld interface of friction welded AISI/SAE 1045 steel bars. Experimentally measured power and axial displacement data were used in conjunction with a finite element transient thermal model to predict the time-temperature history within the heat-affected zone (HAZ) of the weld. This was then used with a microstructure evolution model to predict the volume fraction of the subsequent microconstituents and the microhardness distribution across the weld interface of welds produced using three significantly different welding conditions; one with optimal conditions, one with a long burn-off time and one with high axial pressure and rotational speed but short burn-off time, *i.e.*, hard and fast.

Direct comparison between the predicted and the measured time-temperature history was only possible provided the axial displacement of the weld metal and thermocouples that takes place during the burn-off stage of the friction weld was incorporated in the transient thermal model. In the present study, an algorithm was developed that used measured axial displacements of the weld specimens versus time to correct the predicted time-temperature histories for displacement of the specimens during welding.

To prevent prediction of unrealistic temperature increases at the weld interface, the temperature predicted by the transient thermal model at the weld interface must be restricted to a maximum value, T_{max}. The most appropriate value of T_{max} was found to dependent on the welding conditions, but all were less than the melting temperature of AISI/SAE 1045 steel. Overall there was good agreement between the predicted and the measured time-temperature histories.

In the present study, a calibration procedure for Kirkaldy *et al.*'s[15,16,17] microstructure evolution model which uses existing IT diagrams of the steel of interest has been demonstrated. This calibration procedure ensures that the microstructure model can be used for any steel composition for which an IT diagram exists. Using the predicted time-temperature histories, the calibrated microstructure evolution model was able to predict the effects of the weld process parameters on the resultant width of the HAZ, the volume fractions of the post-weld microconstituents and the microhardness distribution in AISI/SAE 1045 steel friction welds produced using three significantly different sets of welding conditions.

ACKNOWLEDGMENTS

We gratefully acknowledge the financial support received for this study from ARD Industries Ltd., Cambridge, ON Canada, the Ontario Centre for Materials Research (OCMR), the Natural Sciences and Research Council of Canada (NSERC) and the University of Waterloo.

REFERENCES

1. G. Krauss: *Steels – Heat Treatment and Processing Principles*, 1st ed., ASM Int'l, Materials Park, OH, 1990.
2. V.I. Vill: *Welding Production (translated from Russian)*, 1959, vol. 6, pp. 31-41.
3. G.J. Bendzsak and T.H. North: *Trans. JWRI*, 1996, vol. 25 (2), pp. 171-84.
4. N.N. Rykalin, A.I. Pugin, and V.A. Vasil'eva: *Welding Production (translated from Russian)*, 1959, vol. 6, pp. 42-45.
5. YU.D. Potapov, V.V. Trutnev, A. Yakushin, and A.P. Khokhabushin: *Welding Production (translated from Russian)*, 1979, vol. 18 (2), pp. 1-3.
6. T. Rich and R. Roberts: *Metal Construction and British Welding J.*, 1971, vol. 3 (3), pp. 93-98.
7. C.J. Cheng: *Welding J.*, 1962, vol. 41 (12), pp. 542s-50s.
8. O.T. Midling and Ø. Grong: *Acta Metall.*, 1994, vol. 42 (5), pp. 1594-609.
9. I.L.H. Hansson and J.K. Kristensen: *Proc. Int. Conf. on Joining of Metals*, O.A.K. Al-Erhayem, ed., Helsingφr, Denmark, 1984, pp. 161-67.
10. P.G. Bastien, J. Dollet, and Ph. Maynier: *Metal Construction and British Welding J.*, 1970, vol. 2 (9), pp. 9-15.
11. Ph. Maynier, J. Dollet, and P.G. Bastien: *Hardenability Concepts with Applications to Steel*, D.V. Doane and J.S. Kirkaldy, ed., Metallurgical Society of AIME, New York, NY, 1978, pp. 163-76.
12. Ph. Maynier, B. Jungmann, and J. Dollet: *Hardenability Concepts with Applications to Steel*, D.V. Doane and J.S. Kirkaldy, ed., Metallurgical Society of AIME, New York, NY, 1978, pp. 518-44.
13. M.F. Ashby and K.E. Easterling: *Acta Metall.*, 1982, vol. 30 (11), pp. 1969-78.
14. J.C. Ion, K.E. Easterling, and M.F. Ashby: *Acta Metall.*, 1984, vol. 32 (11), pp. 1949-62.
15. J.S. Kirkaldy: *Metall. Trans.*, 1973, vol. 4 (10), pp. 2327-33.
16. J.S. Kirkaldy and R.C. Sharma: *Scripta Metall.*, 1982, vol. 16 (10), pp. 1193-98.
17. J.S. Kirkaldy and D. Venugopalan: *Phase Transformation in Ferrous Alloys*, A.R. Marder and J.I. Goldenstein, ed., Am. Inst. Min. Engrs., Philadelphia, PA, 1984, pp. 125-48.
18. T.C. Nguyen: M.A.Sc. Thesis, University of Waterloo, Waterloo, ON, Canada, 1997.
19. J. Huber: A.R.D. Industries Ltd., Cambridge, ON, Canada, private communication, 1996.
20. G.F. Vander Voort: *Metallography Principles and Practice*, ASM Int'l, Materials Park, OH, 1999.
21. F.P. Incropera and D.P. DeWitt: *Fundamentals of Heat and Mass Transfer*, 3rd ed., John Wiley & Sons, Toronto, ON, 1990, p. 58.
22. R.D. Pelhlke, A. Jeyarajan, and H. Wada: Report No. NSF/MAE-82028, NSF Applied Research Division, University of Michigan, 1982.
23. D.F. Watt, L. Coon, M. Bibby, J. Goldak, and C. Henwood: *Acta Metall.*, 1988, vol. 36 (11), pp. 3029-35.
24. K.H. Huebner and E.A. Thornton: *The Finite Element Method for Engineers*, 2nd ed., John Wiley and Sons, New York, NY, 1982.
25. S.C. Chapra and R.P. Canale: *Numerical Methods for Engineers*, 2nd ed., McGraw-Hill, Toronto, ON, 1988, pp. 261-69.
26. *E112-88 ASTM Standard*, Annual Book of ASTM Standards, Philadelphia, PA, 1994, vol. 03.01, pp. 227-52.
27. W.C. Leslie: *The Physical Metallurgy of Steels*, McGraw-Hill, New York, NY, 1981.
28. G.E. Linnert: *Welding Metallurgy*, 4th ed., American Welding Society, Miami, FL, 1994, vol. 1, p. 837.
29. L. Coon and D.F. Watt: *Computer Modelling of Fabrication Processes and Constitutive Behaviour of Materials*, J. Too, ed., Am. Inst. Min. Engrs., Philadelphia, PA, 1984, pp. 125-48.
30. C. Henwood, M. Bibby, J. Goldak, and D. Watt: *Acta Metall.*, 1988, vol. 36 (11), pp. 3037-46.
31. B. Buchmayr and J.S. Kirkaldy: *J. Heat Treat.*, 1990, vol. 8 (2), pp. 127-36.
32. *Atlas of Time-Temperature Diagram for Irons and Steels*, G.F. Vander Voort, ed., ASM Int'l, Material Park, OH, 1991, p. 14.
33. I.F. Squires: *British Welding J.*, 1966, vol. 13 (11), pp. 652-57.
34. H.M. Tensi, W. Welz, and M. Schwalm: *Aluminium*, 1982, vol. 58, pp. 515-18.